PHOTONICS Research

Flexible top-illuminated organic photodetector using an ultrathin-metal-based transparent electrode

Yuanhe Wang,[1] Xinyi Li,[1] Shihao Liu,[1] Letian Zhang,[1,2] and Wenfa Xie[1,3]

[1]State Key Laboratory of Integrated Optoelectronics, College of Electronic Science and Engineering, Jilin University, Changchun 130012, China
[2]e-mail: zlt@jlu.edu.cn
[3]e-mail: xiewf@jlu.edu.cn

Received 7 August 2023; revised 9 September 2023; accepted 5 October 2023; posted 6 October 2023 (Doc. ID 502731); published 24 November 2023

Top-illuminated structure facilitates the integration of organic photodetectors (OPDs) into high-resolution flexible wearable light detection systems by allowing the OPDs to be deposited on the bottom readout circuit. However, constructing this structure poses a challenge as it demands metallic electrodes with both high optical transparency and high electrical conductivity. But to achieve practical sheet resistances, most semitransparent metallic electrodes tend to reflect a large portion of incident light instead of allowing it to be absorbed by the photoactive layer of the OPDs. This, in turn, results in reduced photocurrent generation. To address this issue, a semiconducting germanium (Ge) film is introduced into a sliver (Ag) film, effectively reducing its reflectivity by lessening scattering. The Ge film also changes how the Ag film grows, further reducing its absorption by lowering the critical thickness needed for forming a continuous film. This approach yields a 10 nm metallic electrode with a transmittance of 70%, a reflectivity of 12%, and a sheet resistance of 35.5 Ω/□. Using this metallic electrode, flexible OPDs exhibit a high photo-to-dark current ratio of 2.9×10^4 and improved mechanical properties. This finding highlights the benefits of the top-illuminated structure, which effectively reduces losses caused by waveguided modes of the incident light.

https://doi.org/10.1364/PRJ.502731

1. INTRODUCTION

Organic photodetectors (OPDs) offer several advantages over inorganic photodetectors, including high portability, low manufacture cost, and easy integration with existing electronic systems. These benefits make OPDs highly promising for applications such as image scanning, artificial retina implantation, and microfluidic sensors [1–3]. Nevertheless, in order to further enhance their capabilities and address the demands of cutting-edge technologies such as biometric fingerprint scanners and intelligent gesture recognition, there is an urgent need for high-resolution OPD arrays equipped with advanced reading-out circuits to achieve unparalleled levels of accuracy in sensing. Compared to a three-terminal phototransistor, a photodiode with a vertical crossbar structure offers a significantly higher device integration density by distributing the top and bottom electrodes on two different planes within the same substrate area [4]. However, most of the previous studies on photodiodes were typically conducted using bottom-illuminated structures [5–7], where photons pass through a transparent substrate with an ITO electrode deposited on it before being absorbed by the photoactive layers. These structures necessitate sharing the substrate with the readout circuits, limiting the advantage of the photodiode in device integration density. A solution lies in the use of top-illuminated structures, where photons are incident into devices through a transparent top electrode, allowing the deposition of photodiodes on the bottom readout circuit.

Constructing top-illuminated structures relies on preparing a transparent top electrode on organic semiconductors. The optical transparency of this electrode determines how many photons can enter the devices, while its electrical conductivity governs the number of photon-generated carriers that can be extracted as output. Moreover, given the increasing demand for wearable systems with advanced detection capabilities, the flexibility of this top electrode emerges as another critical aspect. Its flexibility allows for the development of wearable OPDs that can conform to various application scenarios, ensuring seamless integration and enhanced performance [8]. In comparison to ITO, Ag nanowires, graphene, and other transparent electrodes extensively reported in the literature [9–16], silver (Ag) or its alloy flexible electrodes have demonstrated their effectiveness as a commercially viable transparent top electrode in commercial foldable smartphones. The semitransparent Ag film offers

advantages in terms of optical transparency, electrical conductivity, mechanical flexibility, and the ability to be deposited on nanoscale organic layers [17–19]. However, when aiming for a practical sheet resistance, an Ag film typically exhibits high reflectivity [13]. It has been demonstrated that this high reflectivity can lead to a strong microcavity effect within the organic optoelectronic devices [20–23]. The microcavity effect can enable narrowband detection and resonance wavelengths far below the optical gap of both donor and acceptor. However, the high reflectivity causes a significant portion of incident light to be reflected rather than being absorbed by the photoactive layer of the OPDs. Additionally, the semitransparent silver electrode's parasitic absorption further contributes to a decrease in device efficiency.

Here, we propose to address this issue by modifying the growth mechanism and optical properties of the Ag semitransparent electrode through the introduction of a semiconductor film made of germanium (Ge). Based on our experimental results, we have observed that the Ge alters the growth of the silver film, shifting it from island growth to layer-by-layer growth. Furthermore, the introduction of the Ge can lead to a reduction in the reflectivity of the Ag film by reducing the concentration of free electrons that are available for elastic scattering. It is demonstrated that a stack of Ag (1 nm)/Ge (1 nm)/Ag (8 nm) (AGA) can be obtained with a sheet resistance of 35.5 Ω/□, a transmittance of 70%, and a reflectivity of 12% at 500 nm. Compared to the flexible device with the pure Ag electrode, the flexible device with Ag/Ge/Ag electrode shows significantly improved efficiency, indicating the potential of the Ag/Ge/Ag electrode for flexible OPDs. Additionally, the study revealed that utilizing the AGA-based top-illuminated device architecture provides significant benefits in terms of increasing the percentage of photons that can be absorbed by the photoactive layer. This, in turn, promotes efficient photocurrent generation and enhances the photo-to-dark current ratio, thus demonstrating the superior performance of this architecture.

2. RESULTS AND DISCUSSION

The malleability of Ag makes it possible to prepare flexible OPDs using a device architecture that includes a reflective Ag electrode and a semitransparent Ag electrode [Fig. 1(a)]. However, since Ag has a high reflectivity [24,25], when a reflective Ag film (>100 nm) and a semitransparent Ag film (<30 nm) are used as the two electrodes of an OPD, a strong microcavity effect occurs [26]. While reducing the thickness of the semitransparent Ag film can help decrease the reflectivity of Ag to some extent, the Ag film must still be thick enough to conduct electricity due to its island growth mode [27,28]. As a result, the performance of OPDs with the device architecture shown in Fig. 1(a) is still limited by the high reflectivity and absorption of the Ag semitransparent electrode.

Figure 1(b) shows the reflective characteristics of a conductive Ag semitransparent electrode [20 nm, labeled as Ag film in Fig. 1(b)]. The Ag film exhibits an average reflectivity of over 60% in the visible wavelength range, which not only creates a strong microcavity with the reflective Ag film (>100 nm) but also reduces the ability of the active layer to produce photocurrent. Figure 1(c) illustrates the absorption characteristics of the

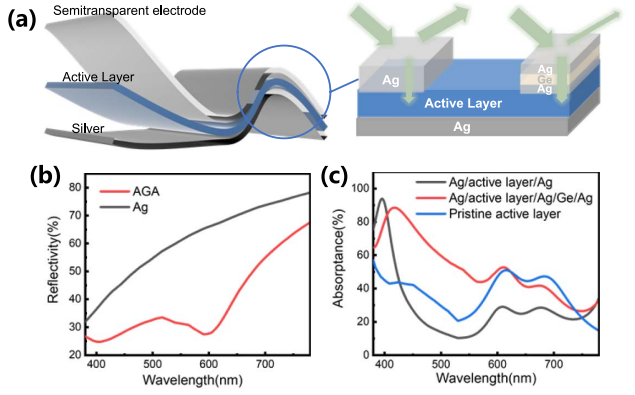

Fig. 1. (a) Structure diagram of flexible OPDs with a reflective Ag electrode and an Ag or AGA semitransparent electrode. (b) Reflectivity characteristics of the Ag film and the AGA film. (c) Absorptance spectra of the photoactive layers consisting of CuPc:C_{60} placed in different device architectures; the blue line represents the active layer without any electrodes, the black line corresponds to the photoactive layer placed in a device with a top electrode of Ag, and the red line indicates the photoactive layer placed in a device with a top electrode of AGA.

active layers consisting of CuPc:50% (mass fraction) C_{60} (20 nm) placed in different device architectures. It can be observed that the Ag/active layer/Ag exhibits much weaker absorption in the wavelength range from 450 to 780 nm. This suggests that most of the incident light is reflected by the Ag semitransparent layer, rather than transmitted into the active layer of the device to produce photocurrent.

To reduce the reflectivity of an Ag semitransparent electrode, a proposed solution is to insert a Ge film with a structure of Ag (15 nm)/Ge (5 nm)/Ag (5 nm). As shown in Fig. 1(b), the reflectivity of the AGA film is significantly lower than that of the Ag film. This is because the Ge film reduces the ability of the Ag film to elastically scatter light. When light strikes the surface of the silver, the free electrons in the metal interact with the electromagnetic waves of the light, causing them to scatter in all directions. It is reasonable to consider that the insertion of a semiconducting Ge film would decrease the concentration of free electrons compared to the pure Ag film, thereby diminishing its scattering capability. When placed in a device with a reflective Ag film (>100 nm) and the semitransparent AGA film, the Ag/active layer/Ag/Ge/Ag exhibits nearly identical absorption characteristics to the pristine active layer in the wavelength range of 550 to 750 nm. This implies that compared to the Ag film, the AGA film allows more photons to pass through and be absorbed by the photoactive layer of the device.

The decreased reflectivity of the AGA semitransparent electrode can significantly enhance the external quantum efficiency (EQE) of the OPDs, as compared to the devices with Ag semitransparent electrodes, since the AGA structure enhances the absorption of photons by the active layer. Figure 2(a) shows the EQE characteristics of the OPDs employing either Ag or AGA films as semitransparent electrodes. The device with a reflective Ag electrode and a semitransparent AGA electrode is denoted as device-AGA, while that with two Ag electrodes is marked as device Ag. As shown in the figure, device AGA

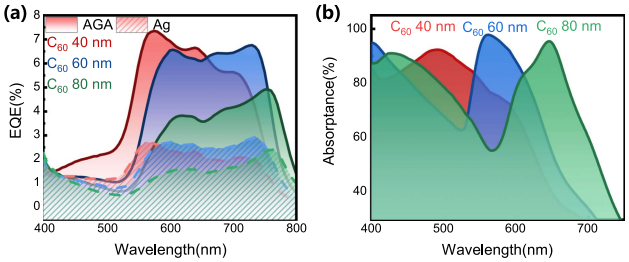

Fig. 2. (a) EQE characteristics of devices Ag and AGA with a device structure: Ag (100 nm)/MoO_3 (5 nm)/CuPc (50 nm)/CuPc:C_{60} (50%, 20 nm)/C_{60} (40, 60, 80 nm)/BCP (10 nm)/Bphen (30 nm)/Ag or AGA (25 nm). The solid curves in the graph depict the characteristics of the AGA device with varying thicknesses of C_{60}, whereas the dashed curves represent the Ag device. The red, blue, and green lines, respectively, represent the EQE characteristics of the devices with C_{60} thicknesses of 40 nm, 60 nm, and 80 nm. (b) Absorptance spectra of devices with C_{60} thicknesses of 40 nm, 60 nm, and 80 nm.

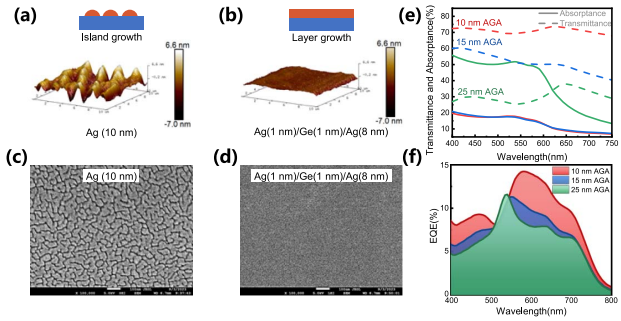

Fig. 3. AFM images and schematic diagram of film growth modes of (a) 10 nm Ag (10 nm) and (b) 10 nm AGA consisting of 1 nm Ag/1 nm Ge/8 nm Ag. SEM images of (c) 10 nm Ag and (d) 10 nm AGA consisting of 1 nm Ag/1 nm Ge/8 nm Ag. (e) Transmittance and absorptance spectra of the AGA films. The red, blue, and green lines, respectively, correspond to AGA films with thicknesses of 10 nm, 15 nm, and 25 nm, respectively. The 10 nm film consists of 1 nm Ag/1 nm Ge/8 nm Ag, the 15 nm film consists of 4 nm Ag/1 nm Ge/10 nm Ag, and the 25 nm film consists of 15 nm Ag/5 nm Ge/5 nm Ag. (f) EQE characteristics of devices with the AGA films with thicknesses of 10 nm, 15 nm, and 25 nm. Its device structure is PET/Ag (100 nm)/MoO_3 (5 nm)/CuPc (20 nm)/CuPc:C_{60}(50 nm)/C_{60} (20 nm)/BCP (10 nm)/Bphen (30 nm)/AGA.

demonstrates significantly higher EQE, with an improvement of more than twice compared to device Ag. This is attributed to the introduction of the Ge film, which reduces the reflection and absorption of the Ag film, thereby enhancing transmittance. Consequently, more photons can be absorbed by the active layer of the AGA, leading to the observed improvement in EQE. It is also noteworthy that as the device thickness increases, the sensitivity of the device to red light becomes more prominent. This can be attributed to the presence of the microcavity effect [Fig. 2(b)], whereby the resonant wavelength experiences a redshift with increasing cavity length. However, even with varying thicknesses of C_{60}, the semitransparent AGA electrode consistently enables higher EQE compared to the semitransparent Ag electrode.

In addition to its high reflectivity, the Ag also causes significant electrode parasitic absorption due to the interaction between photons of light and the electrons in its atomic structure. This absorption limits the EQE of the OPDs. To address this issue, we attempted to reduce the thickness of the Ag film by utilizing the wetting ability of the Ge film to facilitate its film growth. We prepared a 10 nm Ag film and a 10 nm AGA film (consisting of 1 nm Ag/1 nm Ge/8 nm Ag) and observed that the 10 nm AGA film had a sheet resistance of 35.5 Ω/□, whereas the 10 nm Ag film was nonconductive. Figures 3(a) and 3(b) show atomic force microscopy (AFM) images of the 10 nm Ag film and the 10 nm AGA film, respectively. The images visually illustrate the surface morphology of the two films, highlighting the island-like morphology of the 10 nm Ag film and the continuous morphology of the 10 nm AGA film. The island-like morphology displayed by the 10-nm-thick Ag film, as well as the uniform and continuous morphology of the 10 nm AGA film, is further supported by their corresponding scanning electron microscope (SEM) images [see Figs. 3(c) and 3(d)]. When Ag is initially deposited onto a substrate, the adatom mobility is low, resulting in the formation of small, isolated clusters or islands. However, predeposition of a Ge film onto the substrate can create densely packed and smaller nucleation points. This leads to the formation of a continuous Ag film at a much lower thickness because the Ge film acts as a template for efficient nucleation and growth of Ag atoms [29]. The 10 nm AGA film exhibits a significantly higher transmittance and lower absorption [Fig. 3(e)] compared to the 25 nm AGA film, while maintaining a high electrical conductivity. The conductivity of the AGA films with thicknesses of 10, 15, and 25 nm was measured to be 2.8×10^6, 3.4×10^6, and 3.1×10^6 S/m, respectively. These results suggest that variations in composition and thickness do not significantly impact the conductivity of the AGA films. We then prepared three flexible OPDs [refer to Fig. 3(f) caption for more details] using the AGA films with the thicknesses of 10 nm, 15 nm, and 25 nm [Fig. 3(e)]. The 10 nm AGA film, with its improved optical properties, leads to a ∼25% increase in EQE compared to the 25 nm AGA film, as demonstrated in Fig. 3(f).

To assess the mechanical durability of the AGA electrode, we measured the EQE properties of the flexible OPD that used the AGA electrode (marked as flexible device AGA) after subjecting them to 100 and 500 bends, each with a radius of curvature of approximately 2 mm. We found that the flexible OPD exhibits nearly unchanged EQE characteristics after 100 bends, but a 30% reduction in EQE after 500 bends. For comparison, we subjected the flexible device with the ITO electrode (marked as flexible device ITO) to 100 and 500 bends with a radius of curvature of about 2 mm and observed a 15% reduction in EQE after 100 bends, and a 65% reduction in EQE after 500 bends [Fig. 4(a)]. This highlights the superior mechanical stability of the AGA electrode compared to ITO under similar bending conditions. Furthermore, in addition to demonstrating superior mechanical stability, it was also observed that the AGA-based top-illuminated device exhibited a higher photo-to-dark current ratio when compared to ITO-based bottom-illuminated devices. Figure 4(b) illustrates that,

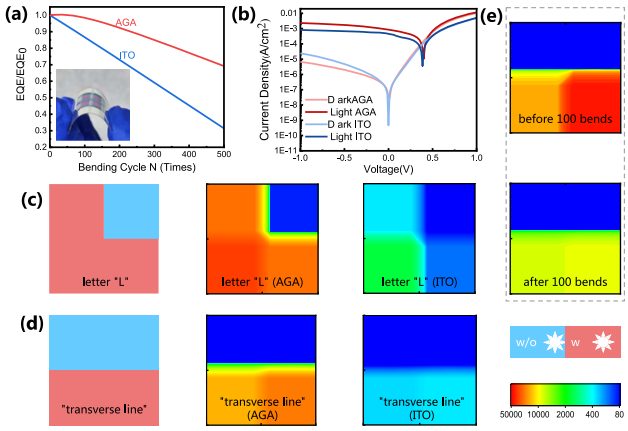

Fig. 4. (a) EQE variation of the flexible OPDs after bending. The flexible device ITO has the same structure as the flexible device AGA, except for the ITO anode and the 100 nm Ag cathode. The insets show the device level diagram. (b) Current density-voltage characteristics of flexible device ITO and flexible device AGA. Imaging of (c) the letter "L" and (d) symbol representing a "transverse line" using 2 × 2 arrays of AGA-based and ITO-based devices, based on photo-to-dark current ratios. The left side shows the schematic diagram, while the right side displays the experimental results. (e) Imaging of a symbol representing a "transverse line" using 2 × 2 arrays of AGA-based devices: before and after 100 bends, based on photo-to-dark current ratios.

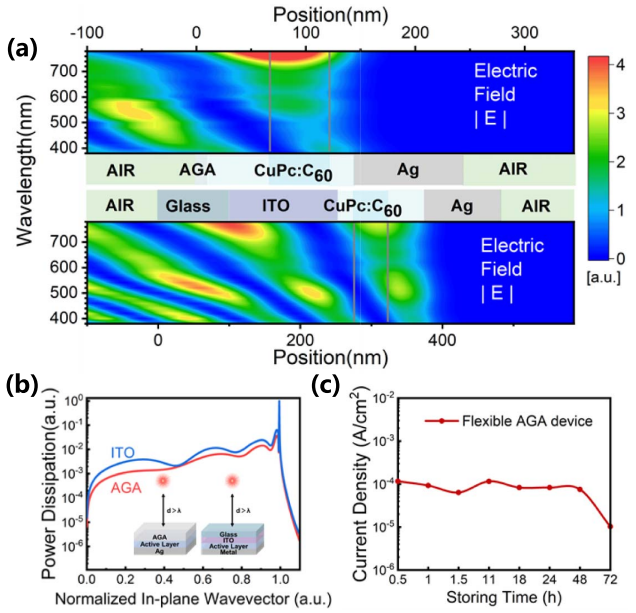

Fig. 5. (a) Simulated electric field intensity $|E|$ and (b) power dissipation characteristics of the AGA-based and the ITO-based devices. The inset shows the schematic diagram of the used simulation model for the calculation of the power dissipation characteristics. (c) Photocurrent characteristics of the organic photodetector with a 10 nm AGA film after exposure to ambient air for varying durations.

when subjected to the same bias voltage, the AGA-based top-illuminated device not only displays a higher photocurrent compared to the ITO-based bottom-illuminated device under the same level of illumination, but also exhibits a lower dark current. The higher photo-to-dark current ratio in AGA-based devices offers an advantage in enhancing the image contrast ratio during imaging. As depicted in Figs. 4(c) and 4(d), two 2 × 2 arrays, one consisting of AGA-based devices and the other consisting of ITO-based devices, were utilized to capture images of a letter "L" [Fig. 4(c)] and a symbol representing a "transverse line" [Fig. 4(d)]. It is evident from the observation that the array utilizing AGA-based devices demonstrates a significantly higher image contrast ratio compared to the array using ITO-based devices. We also performed experiments on imaging flexible photodetectors both before and after bending. The measured results of the flexible AGA device before and after undergoing 100 bends have been included as Fig. 4(e). It is evident that the device both before and after 100 bends was able to capture a symbol representing a "transverse line," although a decrease in imaging contrast was observed after 100 bends.

The reason for the lower dark current observed in the AGA-based device is believed to be the matched working function between the AGA cathode and the Ag anode [29]. On the other hand, in the ITO-based device, the working function of the ITO anode (~4.8 eV) is greater than that of the Ag cathode (~4.3 eV), which results in a nonzero vacuum electrostatic potential. This potential can cause the electric field between the Ag and ITO electrodes to increase in the direction towards the ITO electrode. This results in an increased dark current at negative bias voltages and a decreased injection current at positive bias voltages, as shown in Fig. 4(b). Regarding the higher photocurrent observed in the AGA-based device, it is believed that the device architecture allows for greater photon absorption by the active layer. To investigate this further, we conducted an optical simulation to examine the intensity of the electrical field at different device locations, as shown in Fig. 5. Our simulation revealed that a significant portion of photons become trapped in the glass substrate and ITO electrode in ITO-based devices. This trapped light is a result of the large difference in refractive index between the air/glass, glass/ITO, and ITO/organic semiconductor interfaces. According to the Fresnel equations, this large difference in refractive index causes high reflectivity, which in turn traps the light in waveguided modes. We also conducted calculations to determine the power dissipation characteristics of a dipole source positioned 1 μm ($>\lambda$) away from either the air/AGA interface in the AGA-based device or the glass/ITO interface in the ITO-based device. As depicted in Fig. 5(b), our simulations showed that a larger number of photons was dissipated in the ITO-based device, whereas more photons were absorbed by the AGA-based device. These findings suggest that the AGA-based top-illuminated device architecture is advantageous in increasing the percentage of photons that can be absorbed by the active layer, thereby promoting photocurrent generation. Moreover, it should be noted that ultra-thin silver films are susceptible to oxidation. Therefore, we have assessed the stability of AGA film-based OPDs and observed a gradual decline in device performance after three days of storage in ambient air [see Fig. 5(c)]. However, with the thin film encapsulation technology advancing towards maturity, it is anticipated that it will effectively shield the ultra-thin silver films and organic active

materials from oxidation, thus enabling the stable operation of AGA film-based OPDs.

3. CONCLUSION

To enhance the transmittance of the Ag film and reduce its reflectivity and absorption, a semiconducting Ge film is introduced into it. The Ge film not only reduces the scattering ability of the Ag film by decreasing the concentration of free electrons, but also alters its growth mode to form a continuous Ag film with a much lower thickness. As a result, a 10 nm semitransparent AGA electrode consisting of 1 nm Ag/1 nm Ge/8 nm Ag is successfully prepared with a transmittance of 70% and a sheet resistance of 35 Ω/□. The use of the AGA electrode enables the realization of a flexible top-illuminated OPD with an EQE of 14.2% and a photo-to-dark current ratio of 2.9×10^4. When compared to ITO electrodes, AGA electrodes offer improved mechanical flexibility and photo-to-dark current ratio, demonstrating the advantages of the AGA-based top-illuminated device architecture.

Funding. National Natural Science Foundation of China (62174067, 62175085, 62374071); Science and Technology Development Planning of Jilin Province (20230101061JC).

Disclosures. The authors declare no conflicts of interest related to this paper.

Data Availability. Data underlying the results presented in this paper are not publicly available at this time but may be obtained from the authors upon reasonable request.

REFERENCES

1. T. N. Ng, W. S. Wong, M. L. Chabinyc, S. Sambandan, and R. A. Street, "Flexible image sensor array with bulk heterojunction organic photodiode," Appl. Phys. Lett. **92**, 213303 (2008).
2. G. Simone, D. Di Carlo Rasi, X. de Vries, G. H. Heintges, S. C. Meskers, R. A. Janssen, and G. H. Gelinck, "Near-infrared tandem organic photodiodes for future application in artificial retinal implants," Adv. Mater. **30**, 1804678 (2018).
3. A. Pais, A. Banerjee, D. Klotzkin, and I. Papautsky, "High-sensitivity, disposable lab-on-a-chip with thin-film organic electronics for fluorescence detection," Lab Chip **8**, 794–800 (2008).
4. Y. Liang, Q. Lu, W. Wu, Z. Xu, H. Lu, Z. He, Y. Zhu, Y. Yu, X. Han, and C. Pan, "A universal fabrication strategy for high-resolution perovskite-based photodetector arrays," Small Methods **7**, 2300339 (2023).
5. F. Arca, S. F. Tedde, M. Sramek, J. Rauh, P. Lugli, and O. Hayden, "Interface trap states in organic photodiodes," Sci. Rep. **3**, 1324 (2013).
6. B. Wang, A. D. Scaccabarozzi, H. Wang, M. Koizumi, M. I. Nugraha, Y. Lin, Y. Firdaus, Y. Wang, S. Lee, and T. Yokota, "Molecular doping of near-infrared organic photodetectors for photoplethysmogram sensors," J. Mater. Chem. C **9**, 3129–3135 (2021).
7. C. H. Ji, S. J. Lee, and S. Y. Oh, "P3HT-based visible-light organic photodetectors using PEI/PAA multilayers as a p-type buffer layer," RSC Adv. **9**, 37180–37187 (2019).
8. G. J. Lee, C. Choi, D. H. Kim, and Y. M. Song, "Bioinspired artificial eyes: optic components, digital cameras, and visual prostheses," Adv. Funct. Mater. **28**, 1705202 (2018).
9. C.-J. Lim, J.-H. Kim, and J.-W. Park, "Highly flexible and solution-processed organic photodiodes and their application to optical luminescent oxygen sensors," Org. Electron. **65**, 100–109 (2019).
10. X. Fan, "Doping and design of flexible transparent electrodes for high-performance flexible organic solar cells: recent advances and perspectives," Adv. Funct. Mater. **31**, 2009399 (2021).
11. Y. H. Lee, S. Park, Y. Won, J. Mun, J. H. Ha, J. H. Lee, S. H. Lee, J. Park, J. Yeom, and J. Rho, "Flexible high-performance graphene hybrid photodetectors functionalized with gold nanostars and perovskites," NPG Asia Mater. **12**, 79 (2020).
12. L. Shi, Y. Cui, Y. Gao, W. Wang, Y. Zhang, F. Zhu, and Y. Hao, "High performance ultrathin MoO_3/Ag transparent electrode and its application in semitransparent organic solar cells," Nanomaterials **8**, 473 (2018).
13. H. Yu, H. Zhu, M. Xu, J. Zhang, H. Feng, L. Zhang, S. Liu, and W. Xie, "High-efficiency, large-area, flexible top-emitting quantum-dot light-emitting diode," ACS Photon. **10**, 2192–2200 (2023).
14. S. Kim, S. Y. Kim, J. Kim, and J. H. Kim, "Highly reliable AgNW/PEDOT: PSS hybrid films: efficient methods for enhancing transparency and lowering resistance and haziness," J. Mater. Chem. C **2**, 5636–5643 (2014).
15. W. Liu, B. L. Jackson, J. Zhu, C.-Q. Miao, C.-H. Chung, Y.-J. Park, K. Sun, J. Woo, and Y.-H. Xie, "Large scale pattern graphene electrode for high performance in transparent organic single crystal field-effect transistors," ACS Nano **4**, 3927–3932 (2010).
16. Y. Tang, R. Li, R. Sun, J. Min, Q. Lin, C. Yang, and G. Xie, "Flexible all-organic photodetectors via universal water-assisted transfer printing," The Innovation **4**, 100460 (2023).
17. Q. Zhang, M. Xu, L. Zhou, S. Liu, W. Wang, L. Zhang, W. Xie, and C. Yu, "A flexible organic mechanoluminophore device," Nat. Commun. **14**, 1257 (2023).
18. C. Zang, S. Liu, M. Xu, R. Wang, C. Cao, Z. Zhu, J. Zhang, H. Wang, L. Zhang, W. Xie, and C. Lee, "Top-emitting thermally activated delayed fluorescence organic light-emitting devices with weak light-matter coupling," Light Sci. Appl. **10**, 116 (2021).
19. T. Pan, S. Liu, L. Zhang, W. Xie, and C. Yu, "A flexible, multifunctional, optoeletronic anticounterfeiting device from high-performance organic light-emitting paper," Light Sci. Appl. **11**, 59 (2022).
20. J. Zhang, Y. Wang, S. Liu, H. Yu, L. Zhang, and W. Xie, "Color-tunable organic light-emitting diodes with ultrathin thermal activation delayed fluorescence emitting layer," Appl. Phys. Lett. **120**, 171102 (2022).
21. M. Yin, Z. Yu, T. Pan, X. Peng, X. Zhang, L. Zhang, and W. Xie, "Efficient and angle-stable white top-emitting organic light emitting devices with patterned quantum dots down-conversion films," Org. Electron. **56**, 46–50 (2018).
22. X. Zhang, T. Pan, J. Zhang, L. Zhang, S. Liu, and W. Xie, "Color-tunable, spectra-stable flexible white top-emitting organic light-emitting devices based on alternating current driven and dual-microcavity technology," ACS Photon. **6**, 2350–2357 (2019).
23. B. Siegmund, A. Mischok, J. Benduhn, O. Zeika, S. Ullbrich, F. Nehm, M. Böhm, D. Spoltore, H. Fröb, and C. Körner, "Organic narrowband near-infrared photodetectors based on intermolecular charge-transfer absorption," Nat. Commun. **8**, 15421 (2017).
24. I. Y. Hong, A. B. M. H. Islam, T. K. Kim, Y.-J. Cha, and J. S. Kwak, "Impact of grain growth of silver reflective electrode by electron bombardment on external quantum efficiency of III-nitride micro-light-emitting diode arrays," Appl. Surf. Sci. **512**, 145698 (2020).
25. J. Domaradzki, D. Kaczmarek, M. Mazur, D. Wojcieszak, J. Halarewicz, S. Glodek, and P. Domanowski, "Investigations of optical and surface properties of Ag single thin film coating as semitransparent heat reflective mirror," Mater. Sci. Poland **34**, 747–753 (2016).
26. Y. Li, J. Tang, Z. Xie, L. Hung, and S. Lau, "An efficient organic light-emitting diode with silver electrodes," Chem. Phys. Lett. **386**, 128–131 (2004).
27. K. Aslan, S. N. Malyn, Y. Zhang, and C. D. Geddes, "Conversion of just-continuous metallic films to large particulate substrates for metal-enhanced fluorescence," J. Appl. Phys. **103**, 084307 (2008).
28. X. Sun, J. Dou, F. Xie, Y. Li, and M. Wei, "One-step preparation of mirror-like NiS nanosheets on ITO for the efficient counter electrode of dye-sensitized solar cells," Chem. Commun. **50**, 9869–9871 (2014).
29. S. Liu, W. Liu, J. Yu, W. Zhang, L. Zhang, X. Wen, Y. Yin, and W. Xie, "Silver/germanium/silver: an effective transparent electrode for flexible organic light-emitting devices," J. Mater. Chem. C **2**, 835–840 (2014).